Data report: petrography and phase analyses in lavas and dikes from Hole 1256D (ODP Leg 206 and IODP Expedition 309, East Pacific Rise)[1]

Wanja Dziony,[2] Jürgen Koepke,[2] and François Holtz[2]

Chapter contents

[1] Dziony, W., Koepke, J., and Holtz, F., 2008. Data report: petrography and phase analyses in lavas and dikes from Hole 1256D (ODP Leg 206 and IODP Expedition 309, East Pacific Rise). *In* Teagle, D.A.H., Alt, J.C., Umino, S., Miyashita, S., Banerjee, N.R., Wilson, D.S., and the Expedition 309/312 Scientists, *Proc. IODP,* 309/312: Washington, DC (Integrated Ocean Drilling Program Management International, Inc.).
doi:10.2204/iodp.proc.309312.201.2008

[2] Institut fuer Mineralogie, Leibniz University Hannover, Callinstr. 3, 30167 Hannover, Germany.
Correspondence author:
w.dziony@mineralogie.uni-hannover.de

Abstract

We investigated 56 basalts drilled in Hole 1256D (equatorial East Pacific Rise) during Ocean Drilling Program Leg 206 and Integrated Ocean Drilling Program Expedition 309. Primary magmatic phases, pyroxenes, plagioclases, and Fe-Ti oxides were analyzed in 16 selected samples by electron microprobe analysis. Both clinopyroxene and plagioclase show strong zoning effects, especially in the outermost rims. Many clinopyroxenes show marked zoning, which is in part developed as sector zoning. Some clinopyroxenes bear cores of relict pigeonites, which show slightly higher Mg# (100 * molar MgO/[MgO + FeO^{tot}], where FeO^{tot} = total FeO) than the host crystals. Plagioclase shows a broad scattering in composition, often combined with zoning. We observed a slight trend toward more evolved compositions of mineral phases in the sheeted dikes. Only 1 of the 16 samples bears coexisting magnetite and ilmenite (from the uppermost volcanic unit, the lava pond). By applying the magnetite-ilmenite thermooxybarometer, we calculated an oxygen fugacity corresponding to ΔFMQ of –0.4 (0.4 log units below the oxygen fugacity of the fayalite-magnetite-quartz buffer).

Introduction

Integrated Ocean Drilling Program (IODP) Hole 1256D (6.736°N, 91.934°W), drilled during Ocean Drilling Program (ODP) Leg 206 and IODP Expedition 309/312 (Wilson et al., 2006) is located on 15 Ma oceanic crust formed at the superfast spreading East Pacific Rise (220 mm/y full spreading rate) (Wilson, 1996) on the Cocos plate in the eastern equatorial Pacific. This site was initially chosen to exploit the inverse relationship between spreading rate and depth to axial low-velocity zones, thought to be magma chambers now frozen as gabbros, observed from seismic experiments (Wilson et al., 2006). Hole 1256D penetrated the entire upper oceanic crust and finally drilled into the uppermost gabbro. Site 1256 is a potential location for a complete penetration of the entire ocean crust in the frame of a "mission," a new operational tool of IODP ("Mission Moho") (Christie et al., 2006; Dick et al., 2006). Initial results of drilling at Site 1256, including detailed site maps and information about the geological setting, can be found in the **"Expedition 309/312 summary"** chapter and Teagle, Wilson, Acton, and Vanko (2007). The first individual scientific results con-

doi:10.2204/iodp.proc.309312.201.2008

cerning the structure/composition of the extrusive rocks and details of the hydrothermal alteration within the lavas and dikes are now available (Busigny et al., 2005; Laverne et al., 2006). In this study, 56 samples of the overlying basaltic lava flows and sheeted dikes, drilled during Leg 206 and Expedition 309, were investigated by light microscope and electron microprobe analyses.

Methods and materials

Petrographic data were collected from 56 thin sections covering the depth range from 324 to 1255 meters below seafloor (mbsf) in the drill hole, including the following lithostratigraphic units: the "lava pond," the inflated flows, the sheet and massive flows, the transition zone, and the upper part of the sheeted dike complex (Fig. **F1**). Concerning petrographic terms and rock names we follow those from the **"Site 1256"** chapter and Wilson, Teagle, Acton, et al. (2003). Phenocryst abundances were estimated by digital images processed in a similar way to that described in the **"Methods"** chapter.

Primary magmatic phases in 16 basalts were analyzed (red points, Fig. **F1**) by using polished thin sections and a Cameca SX 100 electron microprobe equipped with five spectrometers and "Peak sight" software. All measurements were made at 15 kV beam potential and 15 nA beam current, with a focused beam and a count time of 20 s for each element. For some Fe-Ti oxides showing exsolution lamellae, a broad beam 20 µm in diameter was used to obtain the initial unexsoluted composition. Matrix correction was performed according to Pouchou and Pichoir (1991). Limits of detection (in weight percent) are as follows:

SiO_2 in Fe-Ti oxides = 0.05,
TiO_2 in pyroxene = 0.03,
Al_2O_3 in Fe-Ti oxides = 0.09,
Cr_2O_3 in pyroxene = 0.18,
Cr_2O_3 in Fe-Ti oxides = 0.19,
MgO in plagioclase = 0.04,
MgO in Fe-Ti oxides = 0.05,
CaO in Fe-Ti oxides = 0.05,
Na_2O in pyroxene = 0.08,
Na_2O in Fe-Ti oxides = 0.13,
K_2O in silicates = 0.08, and
K_2O in Fe-Ti oxides = 0.13.

For establishing relationships between mineral and bulk compositions, we chose samples for which bulk analyses are available (see the **"Site 1256"** chapter and Teagle, Wilson, Acton, and Vanko, 2007).

Petrographic results

Petrographic results are presented in Table **T1.** As phenocrysts, only clinopyroxene and plagioclase were identified. Olivine seems to have been completely altered to secondary minerals, as we only identified possible olivine pseudomorphoses. In spite of careful investigation by both optical microscope and backscattered electron (BSE) imaging combined with energy-dispersive X-ray (EDX) analyses, we were not able to find fresh olivine in our samples. The primary groundmass is composed of plagioclase, clinopyroxene, and Fe-Ti oxides, and anhedral clinopyroxene fills the interstices between the mostly euhedral plagioclase laths.

Microanalytical results

Compositions of the analyzed primary magmatic phases (clinopyroxene, pigeonite, plagioclase, and Fe-Ti oxides) occurring in the investigated basalts are shown in Table **T2.**

Pyroxenes

Analyzed clinopyroxenes show strong zonation with decreasing Mg# toward the rims. Their core compositions vary between $En_{45}Fs_{19}Wo_{36}$ and $En_{58}Fs_{11}Wo_{31}$ with Mg# varying from 70.4 to 84.1. The rims show marked iron enrichment (Fig. **F2**), with Mg# as low as 42.0, corresponding to a FeO^{tot} concentration of 24.6 wt%. Phenocrysts are slightly more primitive in composition compared to groundmass crystals, as reflected by the slightly higher Mg# (Fig. **F3A**). As expected, the Mg# of the clinopyroxenes correlates with the Mg# of the corresponding bulk rock (Fig. **F3A**).

Relics of pigeonite as cores in augite

Pigeonite has been reported as a groundmass mineral occurring as discrete crystal and thin prismatic cores sandwiched by augite in some lavas (e.g., Crispini et al., 2006; Umino, 2007). Our analyses show that these pigeonites have CaO contents ranging from 4.4 to 5.2 wt%. Mg# of pigeonites in augite ranges from 67.3 to 82.2 and are generally slightly higher than those of the host. Two textural types of pigeonite were observed in the samples:

1. Type I pigeonites (Figs. **F4, F5A**) correspond to those described in Crispini et al. (2006) and Umino (2007) and can be easily observed under the light microscope as elongated prismatic crystals embedded in augite with a sharp contact between the two. Both pigeonite and augite show

strong variations in Mg#. This textural type occurs in the fine-grained samples of Unit 1256D-1, which has been interpreted as a ponded lava flow, as well as in one fine-grained sample (309-1256D-118R-1, 43–48 cm) of the flow–dike transition.

2. Type II pigeonites (Figs. F5B, F5C) show different textural features and were first observed in cryptocrystalline and microcrystalline samples of the sheet flows via BSE images. In contrast to Type I pigeonites, they appear as strongly disrupted, often cloudy diffuse patches in intensely zoned groundmass clinopyroxenes, meaning that single pyroxenes bear one or multiple diffuse cores of pigeonitic composition with a more diffuse contact between each other. Because of the strong zonation of the host clinopyroxene, Type II pigeonite is difficult to detect with the light microscope.

The observation of pigeonite in Hole 1256D is significant. Although low-Ca pyroxene is present in many gabbroic rocks from the plutonic crust of fast-spreading ridges (e.g., Hole 1256D; see the "Site 1256" chapter and Gillis, Mével, Allan, et al., 1993), it is normally not observed as phenocrysts in the corresponding erupted lavas ("the orthopyroxene paradoxon"). Here, low-Ca pyroxene was detected, but only as relics with the composition of pigeonite and not of orthopyroxene, which is the typical low-Ca pyroxene occurring in gabbros. Future studies will shed light on this phenomenon.

Sector zoning

Figure F6 presents a BSE image of clinopyroxene showing two domains that can be distinguished by a small difference in their gray levels. The brighter zone is, relative to the darker zone, enriched in Al, Ti, Cr, and Ca and impoverished in Fe and Mg (Fig. F6). Such zoning is hard to detect during routine microprobe analysis and is probably the reason for the relatively large standard deviations related to some averages (Table T2).

Plagioclase

In general, groundmass plagioclase shows marked zoning, with a significant decrease in An content toward the rims. Although the An content of the cores varies between 55.5 and 69.3 mol%, the rims are much lower in An, ranging from 34.7 to 67.1 mol%. The standard deviation for the analyses are large, and some cores show exceptionally high An contents up to >80 mol%. Figure F7 shows some concentration profiles for An to illustrate zoning trends observed in groundmass plagioclases. An and FeO^{tot} content in the plagioclase are negatively correlated, suggesting the bulk rock evolution trend to more iron-rich composition with increasing differentiation (Fig. F8). This is confirmed by a diagram of An content versus bulk Mg# of the host rocks that shows a positive correlation (Fig. F3B).

Analyzed phenocrysts are significantly enriched in An content relative to the groundmass plagioclase, reaching values up to 83.9 mol% (Figs. F3B, F8). This enrichment implies that these phenocrysts are out of equilibrium with the groundmass, representing obvious crystallization products of more primitive magmas, although rims have lower An (<70.9 mol%). Some plagioclase phenocrysts are completely altered to albite, probably because of secondary hydrothermal alteration.

Fe-Ti oxides

Coexisting magnetite and ilmenite were found in only one sample of the lava pond (Fig. F9). For this sample, equilibration temperature and oxygen fugacity was calculated using the "QUILF" software (Andersen, 1993). Equilibrium temperature was estimated to be 784° ± 95°C, reflecting obvious reequilibration during cooling. Calculated oxygen fugacity corresponds to ΔFMQ of –0.4 (0.4 log units below the oxygen fugacity of the fayalite-magnetite-quartz buffer), which is within the range of oxygen fugacities observed in fresh mid-ocean-ridge basalt (MORB) glasses (Bezos and Humler, 2005).

All other samples contain only titanomagnetite. In the diagram for Fe-Ti oxides (Fig. F10), they plot on the ulvospinel-rich side of the ulvospinel-magnetite solid solution.

Mineral downhole variations

We observed slightly lower iron content and a slightly higher An in plagioclase, along with a higher clinopyroxene Mg# in basalt, in the sheeted dikes, compared to the immediately overlying flows (Fig. F11), but no overall trend directly correlated to depth.

Differentiation trend

Kvassnes et al. (2004) estimated typical differentiation trends for MORB by plotting Mg# of clinopyroxene versus An contents of plagioclase in gabbros from different tectonic settings ("dry" and "wet" fractionation). As expected, our data reveal a trend typical for "dry" fractionation (Fig. F12). Including the corresponding mineral data from the two gabbro

screens in the future will help clarify the genetic relationship between gabbros and basalts from the drilled section.

Acknowledgments

This study used samples provided by the Integrated Ocean Drilling Program. The project is funded by the Deutsche Forschungsgemeinschaft (DFG).

References

Andersen, D.J., Lindsley, D.H., and Davidson, P.M., 1993. QUILF: a Pascal program to assess equilibria among Fe-Mg-Mn-Ti oxides, pyroxenes, olivine, and quartz. *Comp. Geosci.,* 19(9):1333–1350. **doi:10.1016/0098-3004(93)90033-2**

Bezos, A., and Humler, E., 2005. The $Fe^{3+}/\Sigma Fe$ ratios of MORB glasses and their implications for mantle melting. *Geochim. Cosmochim. Acta,* 69(3):711–725. **doi:10.1016/j.gca.2004.07.026**

Busigny, V., Laverne, C., and Bonifacie, M., 2005. Nitrogen content and isotopic composition of oceanic crust at a superfast spreading ridge: a profile in altered basalts from ODP Site 1256, Leg 206. *Geochem., Geophys., Geosyst.,* 6(12):Q02O01. **doi:10.1029/2005GC001020**

Christie, D.M., Ildefonse, B., Abe, N., Arai, S., Bach, W., Blackman, D.K., Duncan, R., Hooft, E., Humphris, S.E., and Miller, D.J., 2006. Mission Moho: formation of oceanic lithosphere. *Eos, Trans. Am. Geophys. Union,* 87(48):539. **doi:10.1029/2006EO480005**

Crispini, L., Tartarotti, P., and Umino, S., 2006. Microstructural features of a subaqueous lava from basaltic crust off the East Pacific Rise (ODP Site 1256, Cocos plate). *Ofioliti,* 31:117–127.

Dick, H.J.B., Natland, J.H., and Ildefonse, B., 2006. Past and future impact of deep drilling in the oceanic crust and mantle. *Oceanography,* 19(4):74–82.

Gillis, K., Mével, C, Allan, J., et al., 1993. *Proc. ODP, Init. Repts.,* 147: College Station, TX (Ocean Drilling Program). **doi:10.2973/odp.proc.ir.147.1993**

Kvassnes, A.J.S., Strand, A.H., Moen-Eikeland, H., and Pedersen, R.B., 2004. The Lyngen Gabbro: the lower crust of an Ordovician incipient arc. *Contrib. Mineral. Petrol.,* 148(3):358–379. **doi:10.1007/s00410-004-0609-8**

Laverne, C., Grauby, O., Alt, J.C., and Bohn, M., 2006. Hydroschorlomite in altered basalts from Hole 1256D, ODP Leg 206: the transition from low-temperature to hydrothermal alteration. *Geochem., Geophys., Geosyst.,* 7(10):Q10003. **doi:10.1029/2005GC001180**

Morimoto, N., Fabries, J., Ferguson, A.K., Ginzburg, I.V., Ross, M., Seifert, F.A., Zussman, J., Aoki, K., and Gottardi, G., 1988. Nomenclature of pyroxenes. *Am. Mineral.,* 73(9–10):1123–1133.

Pouchou, J.-L., and Pichoir, F., 1991. Quantitative analysis of homogeneous of stratified micro-volumes applying the model "PAP." *In:* Heinrich, K.F.J., and Newberry, D.E. (Eds.), *Electron Probe Quantitation:* New York (Plenum), 31–75.

Teagle, D.A.H., Wilson, D.S., Acton, G.D., and Vanko, D.A. (Eds.), 2007. *Proc. ODP., Sci. Results,* 206: College Station, TX (Ocean Drilling Program). **doi:10.2973/odp.proc.sr.206.2007**

Umino, S., 2007. Data report: textural variation of Units 1256C-18 and 1256D-1 lava pond, with special reference to recrystallization of the base of Unit 1256C-18. *In* Teagle, D.A.H., Wilson, D.S., Acton, G.D., and Vanko, D.A. (Eds.), *Proc. ODP, Sci. Results*, 206: College Station, TX (Ocean Drilling Program), 1–32. **doi:10.2973/odp.proc.sr.206.007.2007**

Wilson, D.S., 1996. Fastest known spreading on the Miocene Cocos–Pacific plate boundary. *Geophys. Res. Lett.,* 23(21):3003–3006. **doi:10.1029/96GL02893**

Wilson, D.S., Teagle, D.A.H., Acton, G.D., et al., 2003. *Proc. ODP, Init. Repts.,* 206: College Station, TX (Ocean Drilling Program). **doi:10.2973/odp.proc.ir.206.2003**

Wilson, D.S., Teagle, D.A.H., Alt, J.C., Banerjee, N.R., Umino, S., Miyashita, S., Acton, G.D., Anma, R., Barr, S.R., Belghoul, A., Carlut, J., Christie, D.M., Coggon, R.M., Cooper, K.M., Cordier, C., Crispini, L., Durand, S.R., Einaudi, F., Galli, L., Gao, Y., Geldmacher, J., Gilbert, L.A., Hayman, N.W., Herrero-Bervera, E., Hirano, N., Holter, S., Ingle, S., Jiang, S., Kalberkamp, U. Kerneklian, M., Koepke, J., Laverne, C., Vasquez, H.L.L., Maclennan, J., Morgan, S., Neo, N., Nichols, H.J., Park, S.-H., Reichow, M.K., Sakuyama, T., Sano, T., Sandwell, R., Scheibner, B., Smith-Duque, C.E., Swift, S.A., Tartarotti, P., Tikku, A.A., Tominaga, M., Veloso, E.A., Yamasaki, T., Yamazaki, S., and Ziegler, C., 2006. Drilling to gabbro in intact ocean crust. *Science,* 312(5776):1016–1020. **doi:10.1126/science.1126090**

Initial receipt: 2 January 2008
Acceptance: 23 June 2008
Publication: 6 October 2008
MS 309312-201

Figure F1. Simplified lithostratigraphy according to Teagle, Wilson, Acton, and Vanko (2006), including locations of investigated (white) and analyzed (red) samples.

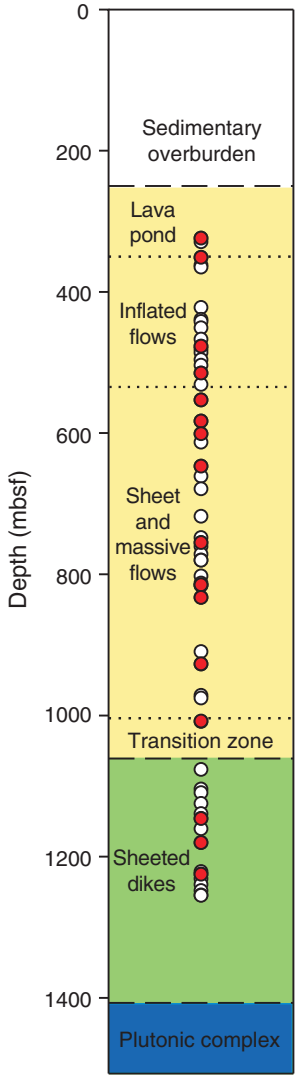

Figure F2. Average compositions of pyroxenes. Quadrilateral after Morimoto et al. (1988). Di = diopside, Hd = hedenbergite, En = enstatite, Fs = ferrosilite.

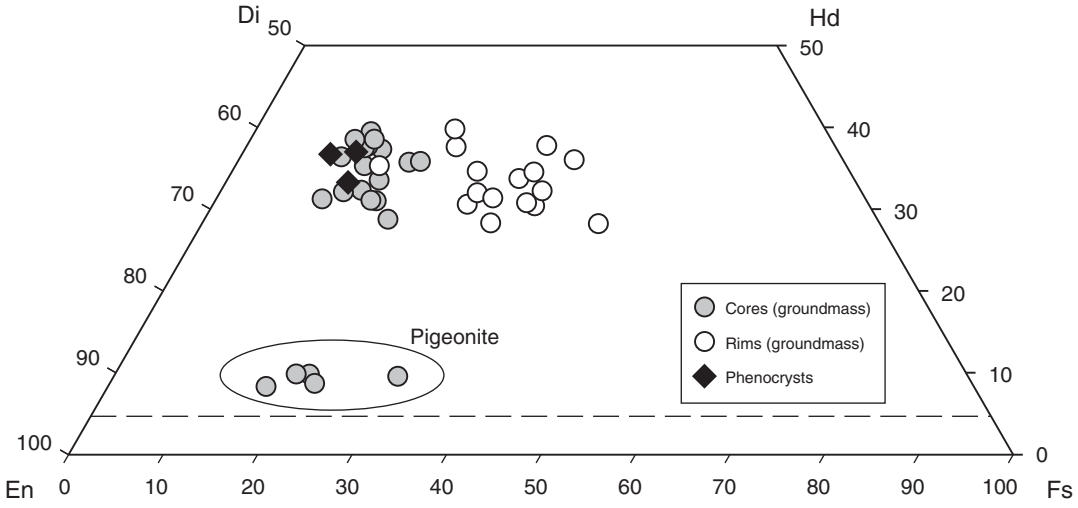

Figure F3. Mg# of clinopyroxene (only core compositions) vs. Mg# of corresponding bulk rock.

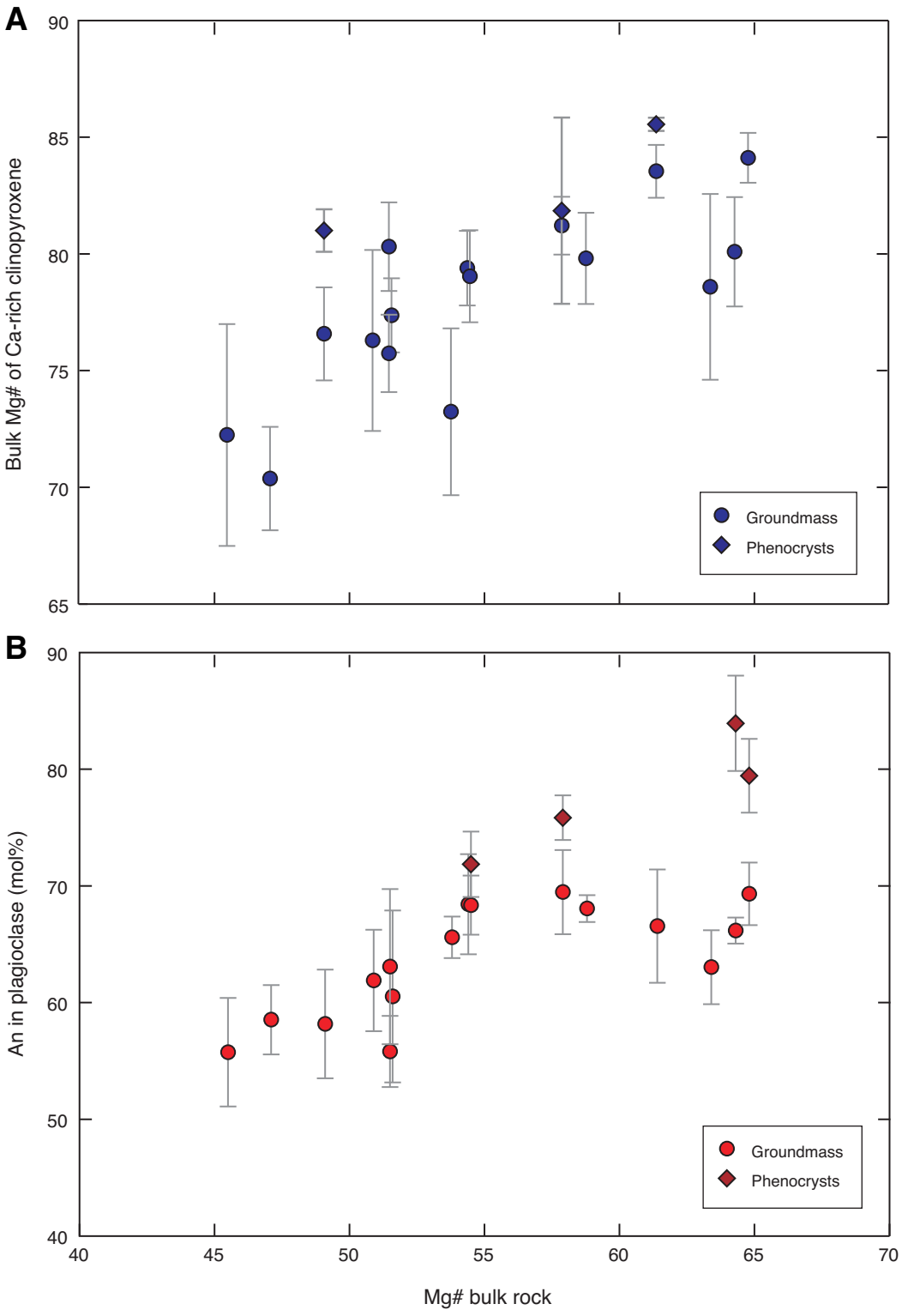

Figure F4. Photomicrograph of groundmass clinopyroxene (cpx) bearing core of Type I relict pigeonite (pgt) (cross-polarized light) (see text for details).

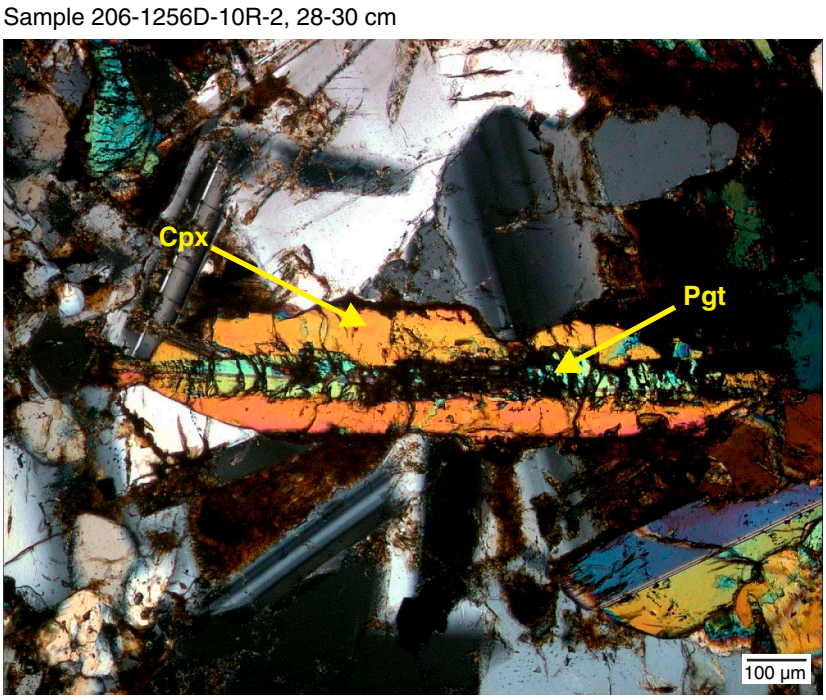

Figure F5. BSE images of clinopyroxene (cpx) with cores of relict pigeonite (pgt). **A.** Type I pigeonite. **B, C.** Type II pigeonite and related electron microprobe profiles (see text for details). Dashed arrows indicate location of profile. pl = plagioclase.

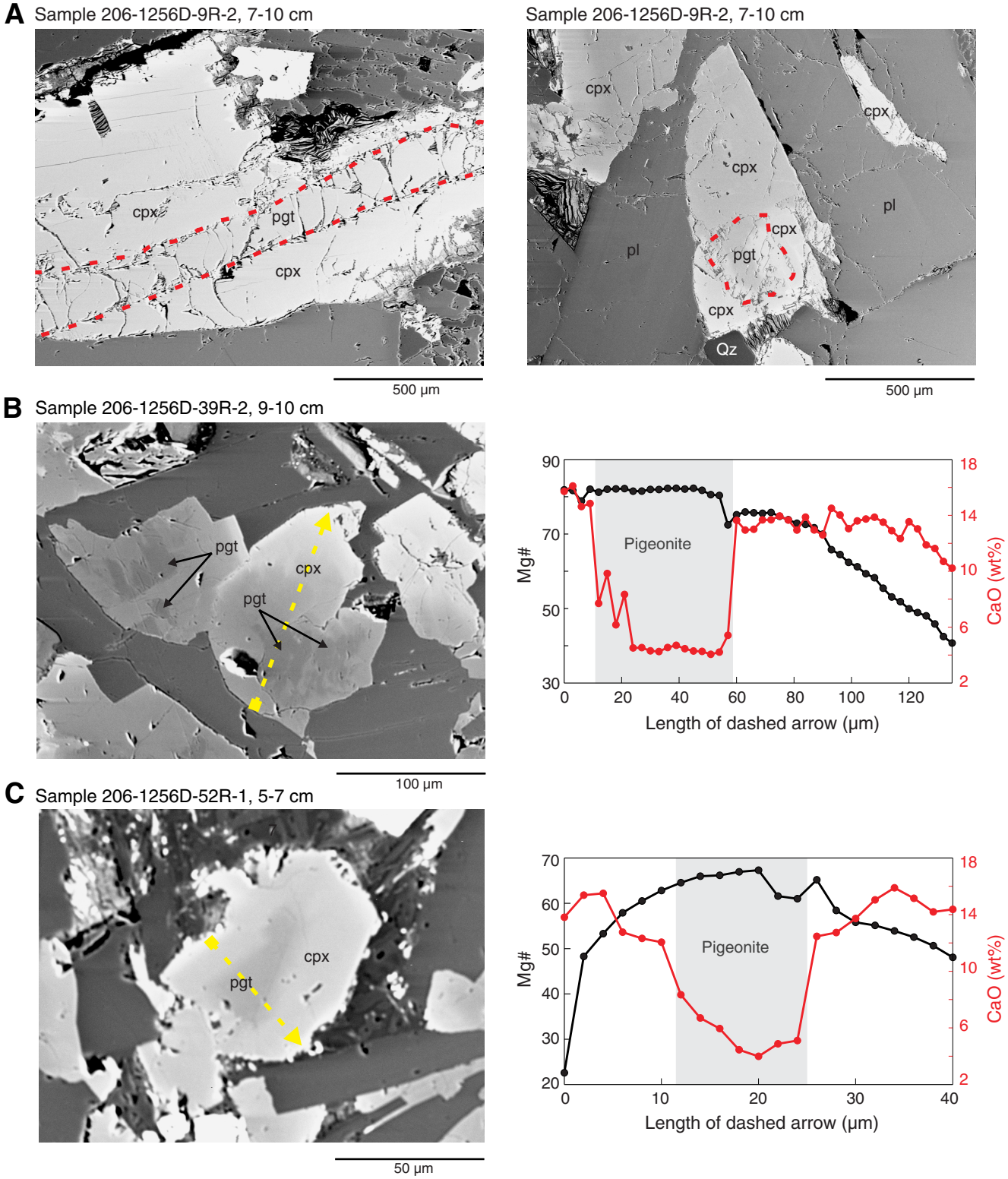

Figure F6. BSE image of clinopyroxene crystal with marked sector zoning. Brighter zone in middle of crystal is relatively enriched in Al, Ti, Cr, and Ca, whereas Fe and Mg are depleted. Dashed arrow indicates location of corresponding microprobe profile through this grain (Fig. F7).

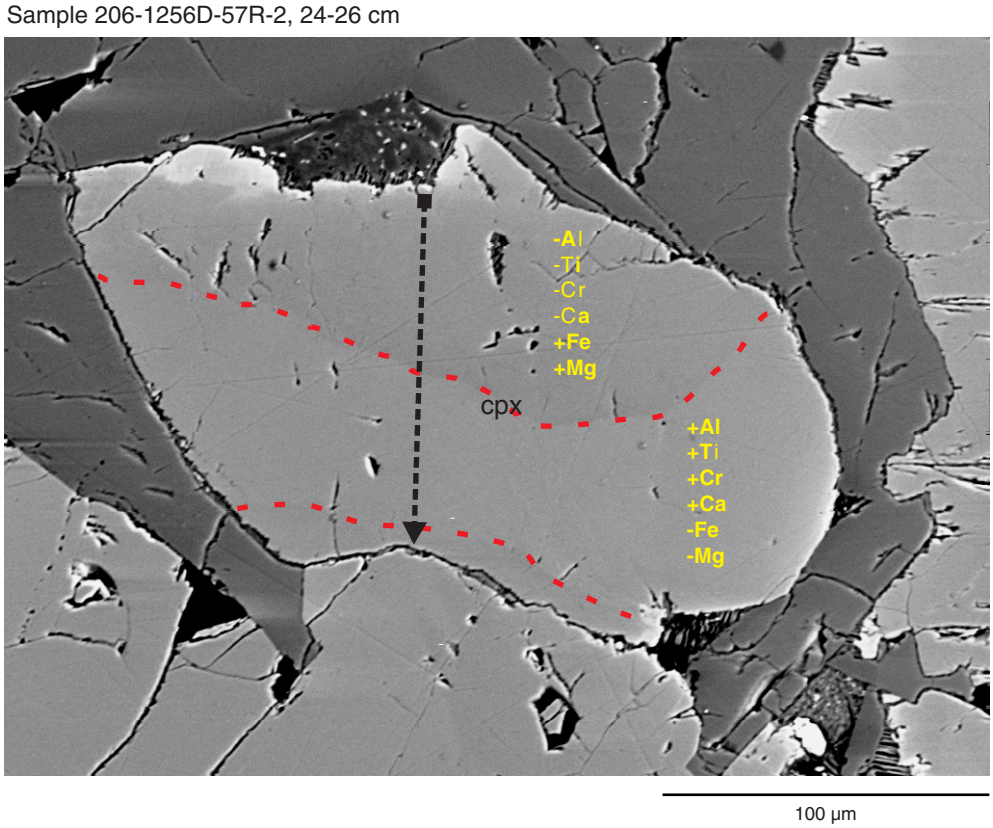

Figure F7. Microprobe profile for elements through clinopyroxene with marked sector zoning shown in Figure F6.

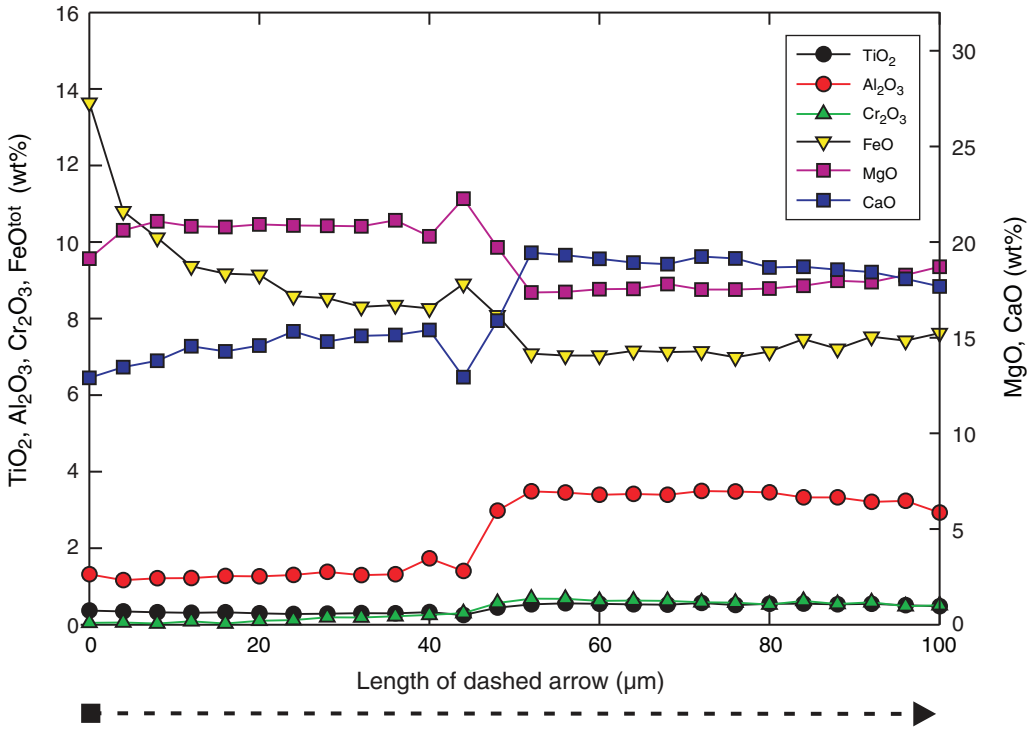

Figure F8. BSE images of groundmass plagioclase (pl) and related electron microprobe profiles for An content. Dashed arrows indicate location of profile.

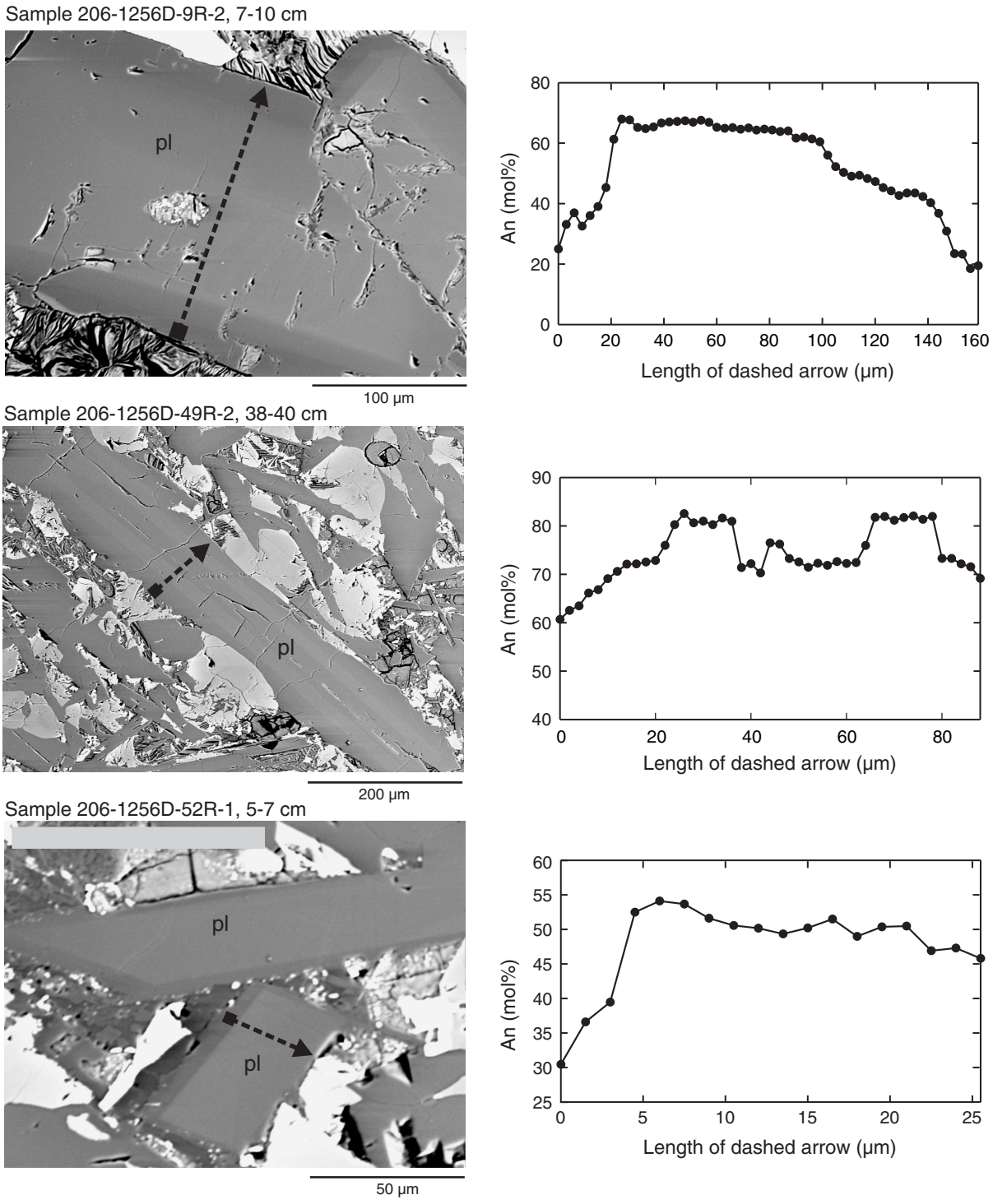

Figure F9. FeO^{tot} in plagioclase vs. An content (only core compositions).

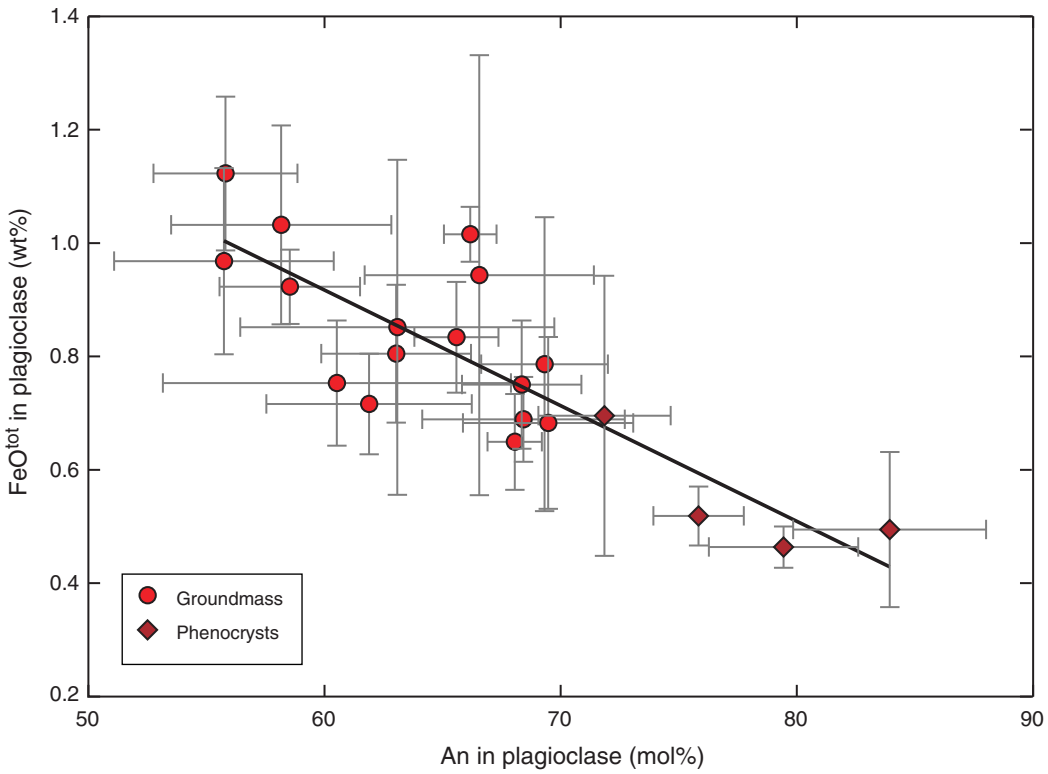

Figure F10. BSE image of oxide cluster with coexisting magnetite (mt) and ilmenite (il).

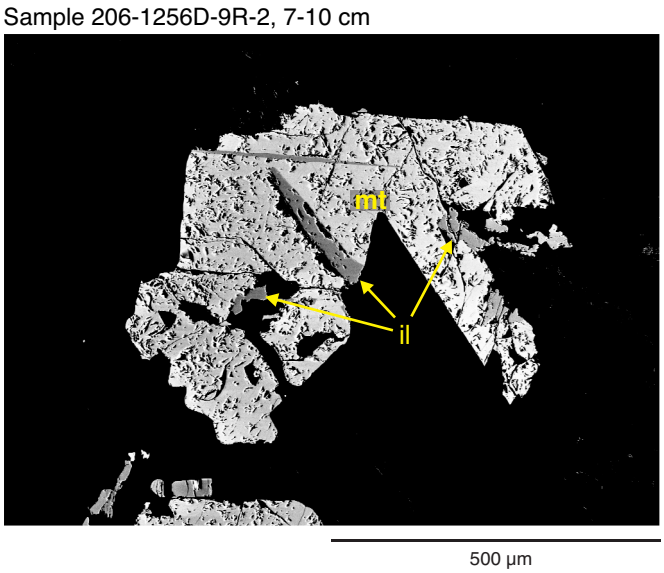

Figure F11. Plot of analyzed magnetites and ilmenites in FeO-Fe_2O_3-TiO_2-ternary diagram.

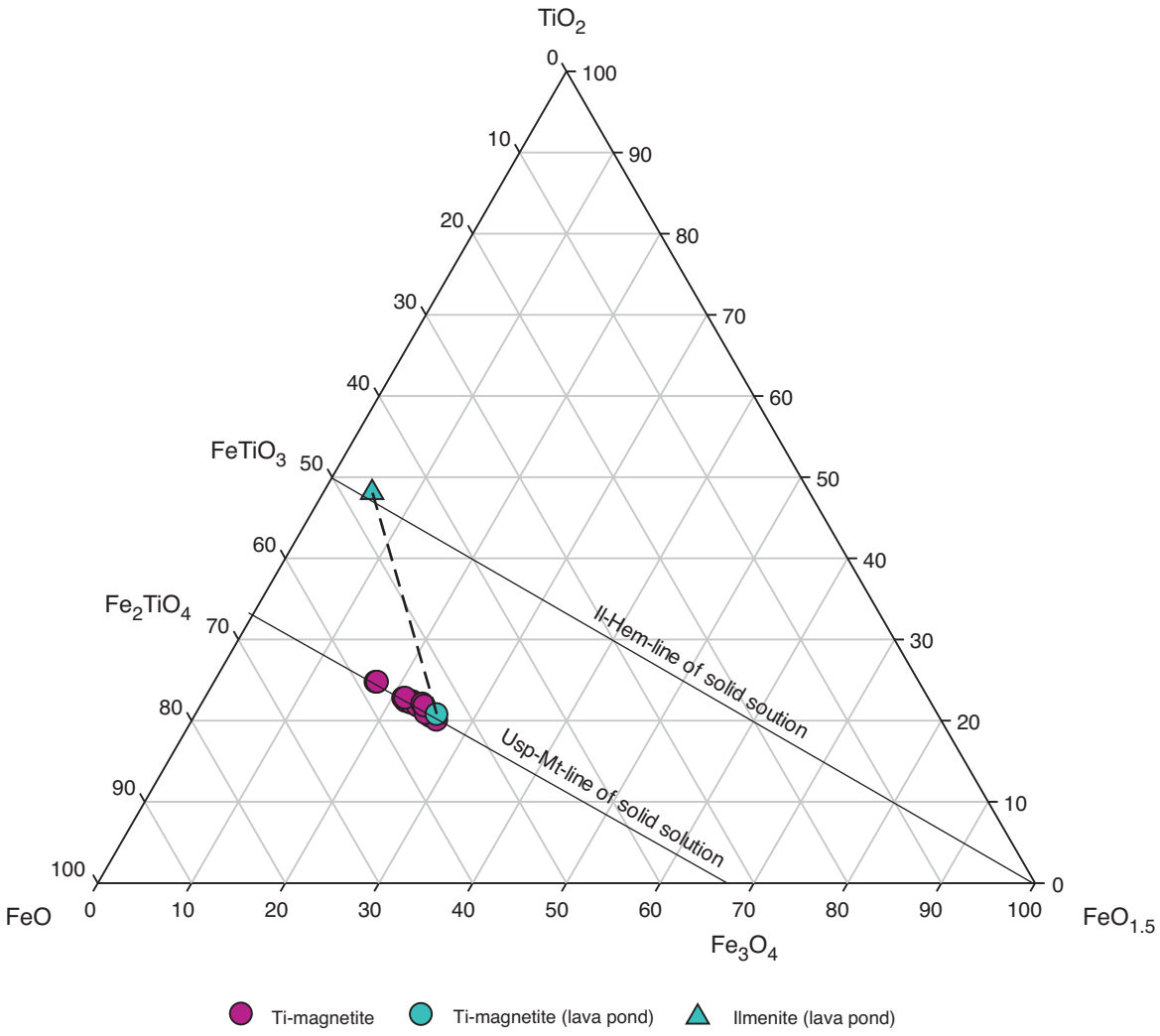

Figure F12. Downhole evolution of An content and FeO^{tot} content of groundmass plagioclase and Mg# of groundmass clinopyroxene.

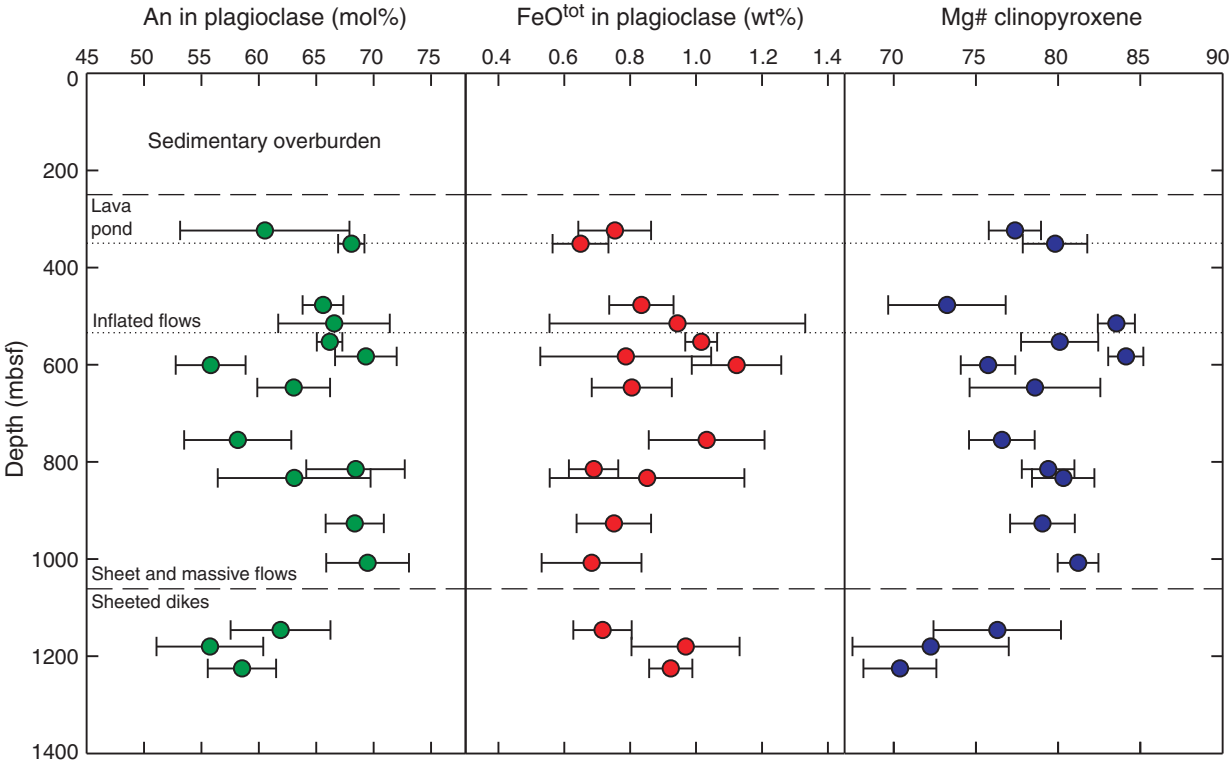

Figure F13. Mg# of clinopyroxene vs. An content of plagioclase plotted against general fractionation trends (redrawn after Kvassnes et al., 2004).

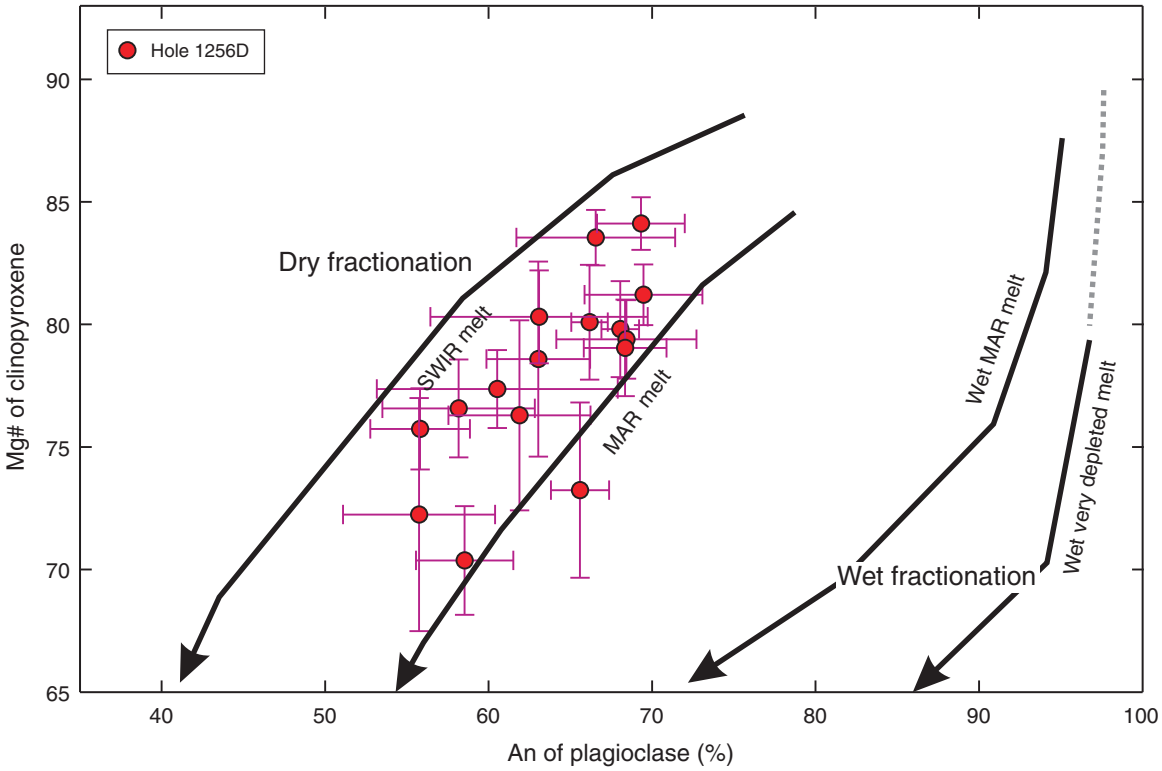

Table T1. Textural features of samples, Hole 1256D. (See table notes.)

Core, section, interval (cm)	Depth CSF (m)	Mode of emplacement	Phenocryst texture	Size	Crystallinity	Texture type	Phenocrysts (%)		
							cpx	pl	Total
206-1256D-									
9R-2, 7–10	324	Ponded lava flow	Aphyric	Fine grained	Hypocrystalline	Intersertal	0.0	0.0	0.0
10R-2, 28–30	329	Ponded lava flow	Aphyric	Fine grained	Hypocrystalline	Intersertal	0.0	0.0	0.0
13R-1, 109–111	351	Massive or sheet flow	Aphyric	Microcrystalline	Hypocrystalline	Intersertal	0.0	0.5	0.5
14R-2, 127–130	362	Massive or sheet flow	Sparsely phyric	Cryptocrystalline	Hypocrystalline	Variolitic	0.0	1.1	1.1
15R-1, 69–71	365	Massive or sheet flow	Aphyric	Cryptocrystalline	Hypocrystalline	Intersertal	0.0	0.0	0.0
24R-2, 119–122	422	Massive or sheet flow	Sparsely phyric	Cryptocrystalline	Hypocrystalline	Intersertal-pilotaxitic	0.5	1.3	1.8
26R-1, 22–24	439	Massive or sheet flow	Aphyric	Cryptocrystalline	Hypocrystalline	Intersertal	0.0	0.0	0.0
26R-4, 17–19	442	Massive or sheet flow	Aphyric	Microcrystalline	Hypocrystalline	Intersertal	0.0	0.0	0.0
28R-1, 33–35	451	Massive or sheet flow	Aphyric	Cryptocrystalline	Hypocrystalline	Variolitic-intersertal	0.0	0.0	0.0
31R-1, 125–127	467	Massive or sheet flow	Aphyric	Cryptocrystalline	Hypocrystalline	Variolitic	0.0	0.0	0.0
32R-6, 6–8	477	Massive or sheet flow	Aphyric	Microcrystalline	Hypocrystalline	Intersertal	0.0	0.0	0.0
33R-1, 32–35	481	Massive or sheet flow	Aphyric	Cryptocrystalline	Hypocrystalline	Variolitic-intersertal	0.0	0.0	0.0
34R-2, 34–37	486	Massive or sheet flow	Aphyric	Cryptocrystalline	Hypocrystalline	Variolitic-intersertal	0.0	0.0	0.0
36R-2, 37–39	496	Massive or sheet flow	Aphyric	Cryptocrystalline	Hypocrystalline	Intersertal	0.0	0.0	0.0
38R-1, 10–14	504	Massive or sheet flow	Aphyric	Cryptocrystalline	Hypocrystalline	Intersertal	0.0	0.0	0.0
39R-2, 9–12	515	Massive or sheet flow	Aphyric	Microcrystalline	Hypocrystalline	Intersertal	0.0	0.0	0.0
42R-2, 31–33	531	Massive or sheet flow	Aphyric	Cryptocrystalline	Hypocrystalline	Variolitic	0.0	0.0	0.0
45R-1, 92–95	553	Massive or sheet flow	Aphyric	Cryptocrystalline	Hypocrystalline	Variolitic-seriate	0.0	0.3	0.3
49R-2, 38–40	583	Massive or sheet flow	Aphyric	Cryptocrystalline	Hypocrystalline	Variolitic-seriate	0.0	0.7	0.7
52R-1, 5–7	601	Massive or sheet flow	Aphyric	Cryptocrystalline	Hypocrystalline	Variolitic	0.0	0.0	0.0
53R-3, 22–24	613	Massive or sheet flow	Aphyric	Cryptocrystalline	Hypocrystalline	Variolitic	0.0	0.0	0.0
57R-2, 24–26	647	Massive or sheet flow	Aphyric	Fine grained	Hypocrystalline	Intersertal	0.0	0.0	0.0
59R-2, 114–115	661	Massive or sheet flow	Sparsely phyric	Cryptocrystalline	Hypocrystalline	Variolitic-glomeroporphyritic	0.8	1.0	1.8
61R-1, 91–96	679	Massive or sheet flow	Aphyric	Cryptocrystalline	Hypocrystalline	Intersertal	0.0	0.0	0.0
67R-3, 60–65	718	Massive or sheet flow	Aphyric	Cryptocrystalline	Hypocrystalline	Variolitic	0.5	0.0	0.5
74R-1, 110–112	748	Massive or sheet flow	Aphyric	Cryptocrystalline	Hypocrystalline	Variolitic-intersertal	0.1	0.0	0.1
309-1256D-									
76R-2, 0–4	755	Massive or sheet flow	Aphyric	Cryptocrystalline	Hypocrystalline	Variolitic	0.2	0.5	0.7
77R-2, 52–55	761	Massive or sheet flow	Moderately phyric	Cryptocrystalline	Hypocrystalline	Variolitic	0.5	2.9	3.5
79R-2,48–50	772	Massive or sheet flow	Aphyric	Cryptocrystalline	Hypocrystalline	Intersertal	0.0	0.0	0.0
80R-1, 55–58	780	Massive or sheet flow	Aphyric	Cryptocrystalline	Hypocrystalline	Variolitic	0.0	0.0	0.0
80R-1, 102–103	780	Massive or sheet flow	Aphyric	Cryptocrystalline	Hypocrystalline	Variolitic	0.0	0.0	0.0
84R-1, 54–56	802	Massive or sheet flow	Aphyric	Cryptocrystalline	Hypocrystalline	Variolitic	0.0	0.0	0.0
85R-1, 116–119	813	Massive or sheet flow	Aphyric	Microcrystalline	Hypocrystalline	Intersertal	0.0	0.0	0.0
85R-3, 76–78	815	Massive or sheet flow	Aphyric	Microcrystalline	Hypocrystalline	Intersertal-subophitic	0.0	0.0	0.0
85R-4, 42–45	816	Massive or sheet flow	Moderately phyric	Cryptocrystalline, fine grained	Hypocrystalline	Variolitic-glomeroporphyritic	0.1	2.1	2.3
87R-2, 63–66	833	Massive or sheet flow	Moderately phyric	Fine grained	Hypocrystalline	Intersertal-subophitic	9.1	0.0	9.1
99R-2, 78–82	909	Massive or sheet flow	Aphyric	Cryptocrystalline	Hypocrystalline	Variolitic	0.0	0.1	0.1
102R-1, 70–72	927	Massive or sheet flow	Aphyric	Microcrystalline, fine grained	Hypocrystalline	Variolitic-intersertal	0.0	0.3	0.3
110R-2, 56–60	972	Massive or sheet flow	Aphyric	Microcrystalline	Hypocrystalline	Intersertal	0.0	0.0	0.0
111R-1, 85–87	975	Massive or sheet flow	Aphyric	Fine grained	Hypocrystalline	Intersertal	0.2	0.3	0.5
118R-1, 45–48	1008	Massive or sheet flow	Sparsely phyric	Fine grained	Hypocrystalline	Intersertal	0.0	1.6	1.6
132R-1, 112–114	1076	Sheeted dike	Aphyric	Cryptocrystalline	Hypocrystalline	Variolitic	0.0	0.0	0.0
138R-1, 10–12	1104	Sheeted dike	Aphyric	Cryptocrystalline	Hypocrystalline	Intersertal	0.0	0.0	0.0
139R-1, 48–50	1109	Sheeted dike	Aphyric	Microcrystalline	Hypocrystalline	Variolitic-intersertal	0.6	0.0	0.6
142R-1, 119–121	1124	Sheeted dike	Aphyric	Fine grained	Hypocrystalline	Intergranular-subophitic	0.0	0.0	0.0
145R-2, 51–55	1139	Sheeted dike	Aphyric	Microcrystalline	Holocrystalline	Intergranular	0.0	0.0	0.0
147R-1, 71–75	1146	Sheeted dike	Aphyric	Fine grained	Holocrystalline	Intergranular	0.0	0.0	0.0
150R-1, 8–10	1160	Sheeted dike	Aphyric	Fine grained	Holocrystalline	Variolitic-intergranular	0.0	0.0	0.0
154R-1, 56–60	1180	Sheeted dike	Aphyric	Microcrystalline	Holocrystalline	Intergranular	0.0	0.0	0.0
163R-3, 59–62	1221	Sheeted dike	Sparsely phyric	Cryptocrystalline	Holocrystalline	Variolitic	0.0	1.0	1.0
164R-2, 115–118	1225	Sheeted dike	Aphyric	Microcrystalline, fine grained	Holocrystalline	Variolitic-intersertal	0.0	0.0	0.0
165R-3, 102–105	1231	Sheeted dike	Aphyric	Microcrystalline	Holocrystalline	Variolitic-intersertal	0.0	0.0	0.0
167R-3, 51–53	1239	Sheeted dike	Aphyric	Cryptocrystalline	Holocrystalline	Variolitic	0.3	0.6	0.9
168R-5, 35–37	1248	Sheeted dike	Aphyric	Microcrystalline	Holocrystalline	Variolitic-intersertal	0.0	0.0	0.0
170R-2, 90–93	1254	Sheeted dike	Sparsely phyric	Cryptocrystalline	Holocrystalline	Variolitic	0.9	0.6	1.5
170R-3, 41–43	1255	Sheeted dike	Aphyric	Microcrystalline	Hypocrystalline	Intersertal-subophitic	0.0	0.0	0.0

Notes: CSF = core depth below seafloor. Aphyric = 0%–1%, sparsely phyric = 1%–5%, moderately phyric = 5%–10%. Cryptocrystalline = <0.1 mm, microcrystalline = 0.1–0.2 mm, fine grained = 0.2–1.0 mm.

Table T2. Average mineral compositions (in weight percent) of selected samples, Hole 1256D. (See table notes.) (Continued on next three pages.)

Core, section, interval (cm)	Lithology	Phase	Analytical method	Number	SiO_2	TiO_2	Al_2O_3	Cr_2O_3	FeO^{tot}	MnO	MgO	CaO	Na_2O	K_2O	Total	Mg#	An
206-1256D-9R-2, 7–10	Ponded lava flow	cpx	Core	8	52.65	0.52	1.85	—	8.96	0.25	17.18	18.51	0.27	—	100.33	77.36	
					0.76	*0.06*	*0.20*		*0.69*	*0.02*	*0.51*	*0.63*	*0.14*			*1.59*	
		cpx	Rim	18	51.31	0.72	1.41	—	16.37	0.43	14.89	14.91	0.23	—	100.27	61.85	
					0.52	*0.08*	*0.21*		*1.75*	*0.06*	*1.33*	*1.47*	*0.03*			*4.08*	
		pgt		17	53.27	0.37	0.88	—	18.95	0.49	21.90	4.82	0.08	—	100.77	67.32	
					0.95	*0.09*	*0.20*		*2.78*	*0.08*	*2.31*	*1.03*	*0.02*		*0.58*	*5.53*	
		pl	Core	5	53.21		28.78		0.75		0.16	12.48	4.50	0.05	99.93		60.36
					2.02		*1.26*		*0.11*		*0.06*	*1.51*	*0.85*	*0.02*			*7.37*
		pl	Rim	5	59.92		25.10		0.48		—	7.25	7.43	0.15	100.33		34.74
					1.92		*1.04*		*0.12*			*1.59*	*0.75*	*0.05*			*7.29*
		ilm	Focused beam	10	—	49.36	0.04	—	47.90	0.54	0.43	—	—	—	98.35		
						0.35	*0.01*		*0.32*	*0.07*	*0.06*						
		mag	Focused beam	21	0.14	20.96	0.86	0.05	71.75	1.00	0.30	—	—	—	95.08		
					0.12	*1.22*	*0.09*	*0.02*	*1.43*	*0.51*	*0.04*						
206-1256D-13R-1, 109–111	Massive or sheet flow	cpx	Core	13	51.22	0.97	3.27	0.23	7.97	0.20	17.69	18.73	0.23	—	100.52	79.81	
					1.49	*0.40*	*1.20*	*0.15*	*0.69*	*0.05*	*1.66*	*1.54*	*0.06*			*1.96*	
		cpx	Rim	6	49.34	1.52	3.24	—	13.36	0.35	13.91	18.12	0.33	—	100.17	64.98	
					0.52	*0.13*	*0.30*		*1.67*	*0.06*	*1.32*	*0.75*	*0.02*			*4.90*	
		pl	Core	9	51.30		30.23		0.65		0.24	14.06	3.65	0.06	100.18		67.83
					0.43		*0.26*		*0.08*		*0.02*	*0.22*	*0.14*	*0.01*			*1.15*
		pl	Rim	4	57.23		26.46		0.78		0.11	9.32	6.22	0.09	100.20		45.07
					2.59		*1.58*		*0.11*		*0.03*	*2.01*	*1.01*	*0.06*			*9.28*
		mag	Focused beam	10	0.14	22.10	1.96	—	68.91	0.61	0.77	0.14	—	—	94.64		
					0.05	*0.41*	*0.14*		*0.52*	*0.05*	*0.12*	*0.03*					
206-1256D-32R-2, 6–8	Massive or sheet flow	cpx	Core	5	52.06	0.53	1.94	—	12.12	0.32	18.61	14.37	0.15	—	100.14	73.24	
					0.50	*0.12*	*0.62*		*2.72*	*0.06*	*1.11*	*2.88*	*0.03*			*3.57*	
		cpx	Rim	3	48.59	0.87	1.33	—	24.63	0.52	10.02	13.20	0.16	—	99.36	42.02	
					0.60	*0.09*	*0.19*		*3.04*	*0.08*	*1.42*	*1.80*	*0.03*			*6.25*	
		pgt		5	54.57	0.20	0.74	—	13.38	0.37	26.07	5.13	—	—	100.56	77.65	
					0.40	*0.05*	*0.13*		*1.11*	*0.04*	*1.46*	*1.98*			*0.36*	*1.53*	
		pl	Core	11	51.99		29.36		0.83		0.23	13.47	3.91	—	99.83		65.59
					0.46		*0.42*		*0.10*		*0.03*	*0.31*	*0.23*				*1.78*
		pl	Rim	3	56.86		25.85		1.25		0.14	9.56	6.08	0.08	99.82		46.28
					1.14		*0.28*		*0.60*		*0.16*	*0.27*	*0.37*	*0.00*			*2.22*
		mag	Focused beam	11	0.17	20.71	1.89	—	71.93	0.48	0.21	0.05	—	—	95.50		
					0.05	*0.39*	*0.20*		*0.39*	*0.07*	*0.05*	*0.03*					
206-1256D-39R-2, 9–10	Massive or sheet flow	cpx	Core	5	52.62	0.37	2.77	0.44	6.70	0.17	19.07	18.24	0.18	—	100.56	83.54	
					0.42	*0.09*	*0.31*	*0.21*	*0.51*	*0.05*	*1.06*	*1.34*	*0.02*			*1.13*	
		cpx	Rim	3	49.33	0.78	1.38	—	20.34	0.47	12.13	14.47	0.18	—	99.11	51.52	
					0.59	*0.17*	*0.46*		*1.92*	*0.01*	*0.21*	*1.64*	*0.04*			*2.60*	
		cpx	Core*	5	53.10	0.23	1.94	0.49	5.90	0.18	19.61	18.60	0.17	—	100.23	85.55	
					0.31	*0.03*	*0.29*	*0.06*	*0.25*	*0.02*	*0.49*	*0.51*	*0.01*			*0.28*	
		pgt		5	55.17	0.11	0.70	—	11.01	0.29	28.38	4.39	—	—	100.17	82.12	
					0.28	*0.01*	*0.06*		*0.40*	*0.04*	*0.13*	*0.19*			*0.42*	*0.54*	
		pl	Core	18	51.68		29.25		0.94		0.30	13.54	3.76	0.04	99.52		66.39
					1.16		*0.94*		*0.39*		*0.19*	*0.99*	*0.57*	*0.01*			*4.85*
		pl	Rim	4	55.52		26.49		1.17		0.13	10.65	5.33	0.08	99.36		52.22
					1.96		*1.10*		*0.34*		*0.18*	*1.24*	*0.76*	*0.02*			*6.48*
		mag	Focused beam	12	0.14	20.09	2.04	—	71.81	0.42	0.26	0.06	—	—	94.89		

Table T2 (continued). (Continued on next page.)

Core, section, interval (cm)	Lithology	Phase	Analytical method	Number	SiO_2	TiO_2	Al_2O_3	Cr_2O_3	FeO^{tot}	MnO	MgO	CaO	Na_2O	K_2O	Total	Mg#	An
					0.02	*0.36*	*0.08*		*0.33*	*0.05*	*0.07*	*0.02*					
206-1256D-45R-1, 92–95	Massive or sheet flow	cpx	Core	7	50.19	1.01	5.18	0.24	7.39	0.18	16.67	18.97	0.19	—	100.02	80.09	
					0.49	*0.09*	*1.04*	*0.15*	*0.96*	*0.03*	*0.72*	*1.01*	*0.02*			*2.34*	
		cpx	Rim	3	49.36	1.23	3.50	—	12.59	0.30	13.51	19.08	0.23	—	99.82	65.66	
					0.90	*0.28*	*0.34*		*2.72*	*0.09*	*2.32*	*0.98*	*0.02*			*8.86*	
		pl	Core	4	52.10		29.42		1.02		0.22	13.60	3.84	0.13	100.33		65.66
					0.21		*0.19*		*0.05*		*0.06*	*0.23*	*0.13*	*0.01*			*1.11*
		pl	Rim	3	54.00		28.10		1.15		0.12	11.89	4.75	0.21	100.22		57.33
					0.39		*0.17*		*0.07*		*0.01*	*0.29*	*0.15*	*0.03*			*1.34*
		pl	Core*	5	47.30		32.89		0.49		0.23	17.21	1.82	0.04	99.99		83.72
					1.25		*0.81*		*0.14*		*0.04*	*0.95*	*0.45*	*0.01*			*4.09*
		pl	Rim*	4	50.93		30.00		0.73		0.30	14.63	3.26	0.08	99.95		70.91
					0.70		*0.43*		*0.13*		*0.03*	*0.51*	*0.30*	*0.02*			*2.55*
206-1256D-49R-2, 38–40	Massive or sheet flow	cpx	Core	13	52.18	0.53	2.73	0.36	6.94	0.21	19.57	17.32	0.19	0.01	100.05	83.40	
					1.32	*0.24*	*1.22*	*0.26*	*0.79*	*0.04*	*1.89*	*2.14*	*0.04*	*0.01*		*1.52*	
		cpx	Rim	2	48.90	1.19	2.73	—	16.18	0.35	13.86	15.16	0.29	—	98.74	60.42	
					1.15	*0.08*	*0.48*		*4.12*	*0.10*	*3.03*	*0.20*	*0.05*			*11.33*	
		pl	Core	6	51.04		29.55		0.79		0.38	14.17	3.47	0.06	99.46		69.06
					0.80		*0.46*		*0.26*		*0.28*	*0.40*	*0.36*	*0.08*			*2.68*
		pl	Rim	5	51.52		29.26		0.80		0.28	13.82	3.71	0.04	99.44		67.13
					0.71		*0.56*		*0.09*		*0.05*	*0.59*	*0.32*	*0.01*			*2.82*
		pl	Core*	5	48.26		31.61		0.46		0.23	16.23	2.32	—	99.14		79.44
					0.98		*0.63*		*0.04*		*0.04*	*0.65*	*0.36*				*3.16*
		pl	Rim*	5	53.50		28.06		0.87		0.22	12.23	4.59	0.06	99.53		59.35
					3.26		*2.45*		*0.22*		*0.15*	*2.67*	*1.50*	*0.04*			*13.17*
206-1256D-52R-1, 5–7	Massive or sheet flow	cpx	Core	7	51.06	0.82	3.26	—	10.55	0.27	18.49	15.35	0.21	—	100.06	75.74	
					0.66	*0.15*	*0.41*		*0.87*	*0.04*	*1.45*	*1.78*	*0.03*			*1.66*	
		cpx	Rim	4	49.42	0.93	1.66	—	20.12	0.48	11.46	15.23	0.21	—	99.52	50.38	
					0.64	*0.29*	*0.56*		*2.70*	*0.10*	*1.61*	*3.39*	*0.06*			*3.87*	
		pgt		6	54.19	0.25	1.05	—	14.26	0.37	26.34	4.58	—	—	101.13	76.70	
					0.90	*0.08*	*0.43*		*2.66*	*0.06*	*2.21*	*0.99*			*0.43*	*4.77*	
		pl	Core	10	54.41		27.60		1.12		0.14	11.41	4.99	0.06	99.73		55.62
					0.67		*0.46*		*0.14*		*0.05*	*0.61*	*0.36*	*0.01*			*3.05*
		pl	Rim	6	59.64		24.72		0.97		—	7.72	6.90	0.12	100.09		37.91
					2.29		*1.13*		*0.16*			*1.63*	*0.81*	*0.06*			*7.83*
		mag	Focused beam	5	0.21	21.79	1.96	—	67.83	0.78	0.18	0.11	—	—	92.93		
					0.16	*0.43*	*0.13*		*0.50*	*0.13*	*0.04*	*0.04*					
206-1256D-57R-2, 24–26	Massive or sheet flow	cpx	Core	4	52.66	0.45	1.99	0.22	9.30	0.27	19.15	16.28	0.17	—	100.49	78.59	
					0.71	*0.15*	*0.86*	*0.33*	*2.32*	*0.04*	*1.51*	*2.79*	*0.04*			*3.98*	
		pl	Core	15	52.55		29.03		0.80		0.20	13.03	4.22	0.05	99.88		62.86
					0.76		*0.45*		*0.12*		*0.04*	*0.67*	*0.36*	*0.01*			*3.17*
		pl	Rim	5	57.80		25.89		0.73		—	9.08	6.45	0.08	100.04		43.54
					0.70		*0.23*		*0.09*			*0.36*	*0.19*	*0.00*			*1.66*
		mag	Focused beam	15	0.30	22.31	1.70	—	70.23	0.95	0.17	0.05	—	—	95.76		
					0.55	*0.79*	*0.20*		*1.23*	*0.22*	*0.10*	*0.05*					
309-1256D-76R-2, 0–4	Massive or sheet flow	cpx	Core	7	51.95	0.59	2.61	—	10.29	0.27	18.88	15.56	0.18	—	100.38	76.57	
					0.71	*0.10*	*0.35*		*1.00*	*0.05*	*1.42*	*1.90*	*0.04*			*1.99*	
		cpx	Rim	5	48.95	1.14	2.11	—	19.69	0.44	12.32	14.61	0.27	—	99.56	52.73	
					0.95	*0.33*	*0.69*		*3.36*	*0.08*	*1.74*	*3.47*	*0.12*			*5.16*	
		cpx	Core*	12	52.98	0.37	2.11	—	8.16	0.24	19.52	16.81	0.18	—	100.50	81.00	
					0.38	*0.05*	*0.26*		*0.98*	*0.05*	*1.31*	*2.38*	*0.03*			*0.91*	

Table T2 (continued). (Continued on next page.)

Core, section, interval (cm)	Lithology	Phase	Analytical method	Number	SiO_2	TiO_2	Al_2O_3	Cr_2O_3	FeO^{tot}	MnO	MgO	CaO	Na_2O	K_2O	Total	Mg#	An
		pgt		3	54.85	0.19	1.00	—	12.56	0.34	26.78	5.17	0.06	—	101.01	79.17	
					0.17	*0.01*	*0.35*		*0.25*	*0.06*	*0.87*	*1.25*	*0.03*			*0.33*	
		pl	Core	6	53.99		27.82		1.03		0.16	11.99	4.76	0.05	99.81		57.99
					1.11		*0.87*		*0.18*		*0.05*	*0.96*	*0.53*	*0.01*			*4.66*
		pl	Rim*	13	52.66		28.87		0.81		0.21	13.14	4.13	0.04	99.86		63.58
					1.48		*1.12*		*0.23*		*0.03*	*1.17*	*0.66*	*0.01*			*5.73*
		mag	Focused beam	5	0.20	22.14	2.25	—	67.40	1.70	—	0.23	—	—	93.99		
					0.04	*0.21*	*0.21*		*1.14*	*0.11*		*0.06*					
309-1256D-85R-3, 76–78	Massive or sheet flow	cpx	Core	7	52.45	0.48	2.46	—	8.32	0.25	17.98	17.31	0.18	—	99.59	79.39	
					1.12	*0.20*	*1.07*		*0.68*	*0.04*	*1.58*	*1.66*	*0.05*			*1.60*	
		cpx	Rim	3	49.43	0.93	2.09	—	18.07	0.40	11.93	15.78	0.23	—	98.87	54.05	
					0.89	*0.09*	*0.49*		*4.46*	*0.13*	*2.94*	*0.39*	*0.05*			*12.32*	
		pl	Core	12	51.01		29.85		0.69		0.27	14.02	3.57	—	99.44		68.43
					1.32		*0.83*		*0.07*		*0.07*	*0.84*	*0.50*				*4.29*
		pl	Rim	12	54.30		27.62		0.93		0.15	11.44	5.01	0.05	99.51		55.61
					2.11		*1.38*		*0.15*		*0.08*	*1.60*	*0.88*	*0.02*			*7.79*
		mag	Focused beam	9	0.14	21.45	2.07	—	68.95	1.73	—	0.08	—	—	94.49		
					0.02	*0.75*	*0.21*		*0.71*	*0.08*		*0.03*					
309-1256D-87R-2, 63–66	Massive or sheet flow	cpx	Core	13	52.15	0.49	2.43	—	7.88	0.22	18.03	18.83	0.20	—	100.38	80.31	
					0.60	*0.11*	*0.60*		*0.74*	*0.03*	*0.83*	*0.80*	*0.02*			*1.90*	
		cpx	Rim	3	49.99	0.78	1.72	—	17.78	0.43	13.78	15.25	0.22	—	99.96	58.01	
					0.76	*0.18*	*0.07*		*1.23*	*0.04*	*3.67*	*4.10*	*0.07*			*7.18*	
		pl	Core	14	52.46		28.54		0.85		0.29	13.05	4.22	0.04	99.44		62.95
					1.81		*1.38*		*0.30*		*0.28*	*1.43*	*0.75*	*0.01*			*6.65*
		pl	Rim	5	58.19		25.59		0.74		—	8.93	6.54	0.06	100.08		42.86
					1.42		*0.86*		*0.10*			*1.09*	*0.59*	*0.01*			*5.18*
		mag	Focused beam	11	0.15	22.60	1.82	—	68.76	1.71	—	0.07	—	—	95.17		
					0.01	*0.46*	*0.28*		*0.72*	*0.07*		*0.02*					
309-1256D-102R-1, 70–72	Massive or sheet flow	cpx	Core	7	50.70	0.77	3.63	0.27	8.01	0.17	16.95	18.80	0.21	—	99.51	79.04	
					0.66	*0.14*	*0.36*	*0.07*	*0.60*	*0.03*	*0.93*	*0.89*	*0.02*			*1.97*	
		cpx	Rim	10	49.43	1.02	2.28	—	18.33	0.42	14.18	13.57	0.19	—	99.45	57.96	
					1.54	*0.36*	*0.34*		*4.87*	*0.11*	*3.81*	*2.63*	*0.03*			*12.92*	
		pl	Core	11	51.44		29.58		0.75		0.27	13.96	3.57	—	99.60		68.35
					0.67		*0.55*		*0.11*		*0.04*	*0.52*	*0.29*				*2.53*
		pl	Rim	7	56.28		26.30		1.02		0.08	10.18	5.63	0.07	99.56		49.76
					1.03		*0.68*		*0.11*		*0.03*	*0.80*	*0.42*	*0.01*			*3.80*
		pl	Core*	6	50.54		30.00		0.70		0.36	14.70	3.18	—	99.51		71.86
					0.82		*0.84*		*0.25*		*0.20*	*0.70*	*0.29*				*2.80*
		pl	Rim*	6	53.47		28.05		0.97		0.20	12.28	4.50	0.04	99.51		59.97
					2.22		*1.60*		*0.25*		*0.05*	*1.91*	*0.98*	*0.02*			*9.02*
		mag	Focused beam	10	0.14	20.59	2.23	—	69.87	1.18	—	0.08	—	—	94.15		
					0.02	*1.00*	*0.29*		*1.04*	*0.07*		*0.04*					
309-1256D-118R-1, 43–48	Massive or sheet flow	cpx	Core	7	52.84	0.37	2.08	0.35	8.25	0.23	20.00	16.29	0.16	—	100.58	81.21	
					1.01	*0.13*	*0.71*	*0.15*	*0.69*	*0.06*	*1.74*	*2.11*	*0.03*			*1.24*	
		cpx	Rim	1	48.83	0.77	1.56	—	19.03	0.48	11.46	16.45	0.22	—	98.82	51.75	
		cpx	Core*	7	51.77	0.36	3.04	0.97	7.31	0.24	18.10	18.26	0.22	—	100.27	81.51	
					0.73	*0.05*	*0.23*	*0.11*	*0.90*	*0.06*	*2.63*	*2.15*	*0.05*			*3.99*	
		pl	Core	9	51.01		29.66		0.68		0.24	14.20	3.45	—	99.27		69.47
					0.99		*0.58*		*0.15*		*0.04*	*0.71*	*0.42*				*3.60*
		pl	Rim	4	56.90		26.16		0.79		0.04	9.67	5.91	0.10	99.57		47.20

Table T2 (continued).

Core, section, interval (cm)	Lithology	Phase	Analytical method	Number	SiO_2	TiO_2	Al_2O_3	Cr_2O_3	FeO^{tot}	MnO	MgO	CaO	Na_2O	K_2O	Total	Mg#	An
					1.30		*0.70*		*0.21*		*0.03*	*1.04*	*0.67*	*0.04*			*5.46*
		pl	Core*	7	49.32		31.30		0.52		0.26	15.60	2.75	—	99.77		75.84
					0.55		*0.36*		*0.05*		*0.04*	*0.43*	*0.22*				*1.91*
		pl	Rim*	4	55.05		27.02		0.81		0.07	10.77	5.44	0.07	99.22		52.04
					0.51		*0.63*		*0.06*		*0.02*	*0.36*	*0.21*	*0.01*			*1.81*
		mag	Focused beam	7	0.69	21.25	2.01	—	67.27	2.50	0.18	0.21	—	—	94.19		
					0.90	*1.31*	*0.33*		*0.62*	*0.17*	*0.36*	*0.11*					
309-1256D-147R-1, 71–75	Sheeted dike	cpx	Core	13	51.93	0.52	2.16	—	10.00	0.28	18.05	16.73	0.20	—	100.02	76.29	
					0.89	*0.14*	*0.60*		*2.15*	*0.05*	*1.21*	*2.28*	*0.03*			*3.88*	
		cpx	Rim	6	50.52	0.60	1.54	—	15.67	0.38	13.69	16.73	0.22	—	99.38	60.88	
					1.28	*0.26*	*0.52*		*5.05*	*0.11*	*4.53*	*1.53*	*0.03*			*16.19*	
		pl	Core	8	52.89		28.69		0.72		0.15	12.71	4.33	0.04	99.52		61.73
					1.02		*0.73*		*0.09*		*0.04*	*0.88*	*0.50*	*0.01*			*4.35*
		mag	Broad beam	2	0.67	23.87	1.77	—	65.14	1.24	0.09	0.55	—	—	93.39		
					0.79	*0.87*	*0.28*		*1.01*	*0.05*	*0.12*	*0.47*					
309-1256D-154R-1, 56–60	Sheeted dike	cpx	Core	11	50.85	0.80	2.69	—	11.21	0.28	16.37	17.65	0.22	—	100.15	72.24	
					0.51	*0.11*	*0.22*		*1.83*	*0.05*	*1.36*	*1.00*	*0.03*			*4.75*	
		cpx	Rim	4	48.99	0.93	1.60	—	20.88	0.51	9.62	16.96	0.22	—	99.75	45.08	
					0.52	*0.11*	*0.24*		*2.01*	*0.04*	*2.18*	*0.78*	*0.03*			*7.76*	
		pl	Core	8	54.43		27.69		0.97		0.12	11.53	5.06	0.06	99.85		55.54
					1.37		*0.82*		*0.16*		*0.05*	*1.00*	*0.51*	*0.01*			*4.65*
		pl	Rim	8	56.80		26.18		1.05		0.09	9.63	6.01	0.08	99.83		46.76
					2.36		*1.23*		*0.37*		*0.11*	*1.62*	*0.83*	*0.02*			*7.61*
		mag	Focused beam	8	0.20	21.16	1.30	—	68.00	2.13	—	0.22	—	—	93.12		
					0.05	*2.08*	*0.47*		*2.81*	*0.44*		*0.05*					
309-1256D-164R-2, 115–118	Sheeted dike	cpx	Core	9	50.81	0.71	2.46	—	11.89	0.29	15.84	17.61	0.24	—	99.87	70.37	
					0.37	*0.10*	*0.25*		*0.76*	*0.03*	*0.92*	*1.06*	*0.02*			*2.22*	
		cpx	Rim	4	49.40	0.82	1.58	—	18.97	0.43	10.47	18.04	0.24	—	99.98	49.58	
					0.66	*0.05*	*0.08*		*2.23*	*0.03*	*1.40*	*0.89*	*0.04*			*6.23*	
		pl	Core	8	53.29		28.20		0.92		0.16	12.04	4.71	0.05	99.36		58.38
					0.79		*0.52*		*0.07*		*0.03*	*0.63*	*0.33*	*0.01*			*2.97*
		pl	Rim	6	58.22		25.49		0.75		—	8.43	6.57	0.11	99.59		41.22
					2.72		*1.53*		*0.21*			*1.85*	*0.93*	*0.07*			*8.86*
		mag	Focused beam	12	1.03	24.08	1.10	—	65.68	0.95	0.13	0.75	—	—	93.79		
					1.14	*1.35*	*0.18*		*2.29*	*0.54*	*0.07*	*1.03*					

Notes: Number = number of phases. One standard deviation is listed below its average composition in italics. cpx = clinopyroxene, pgt = pigeonite, pl = plagioclase, ilm = ilmenite, mag = magnetite. Broad beam analysis was used to reintegrate exsolution lamellae. * = phenocryst. An = mol% content of plagioclase. — = below limit of detection, empty cell = not analyzed.